nature materials

REVIEW ARTICLE
| DOI: 10.1038/NMAT3839

Flat optics with designer metasurfaces

Nanfang Yu[1]* and Federico Capasso[2]*

Conventional optical components such as lenses, waveplates and holograms rely on light propagation over distances much larger than the wavelength to shape wavefronts. In this way substantial changes of the amplitude, phase or polarization of light waves are gradually accumulated along the optical path. This Review focuses on recent developments on flat, ultrathin optical components dubbed 'metasurfaces' that produce abrupt changes over the scale of the free-space wavelength in the phase, amplitude and/or polarization of a light beam. Metasurfaces are generally created by assembling arrays of miniature, anisotropic light scatterers (that is, resonators such as optical antennas). The spacing between antennas and their dimensions are much smaller than the wavelength. As a result the metasurfaces, on account of Huygens principle, are able to mould optical wavefronts into arbitrary shapes with subwavelength resolution by introducing spatial variations in the optical response of the light scatterers. Such gradient metasurfaces go beyond the well-established technology of frequency selective surfaces made of periodic structures and are extending to new spectral regions the functionalities of conventional microwave and millimetre-wave transmit-arrays and reflect-arrays. Metasurfaces can also be created by using ultrathin films of materials with large optical losses. By using the controllable abrupt phase shifts associated with reflection or transmission of light waves at the interface between lossy materials, such metasurfaces operate like optically thin cavities that strongly modify the light spectrum. Technology opportunities in various spectral regions and their potential advantages in replacing existing optical components are discussed.

Optical devices modify the wavefront of light by altering its phase, amplitude and polarization in a desired manner. Conventional optical components are based on refraction, reflection or diffraction of light and wavefront shaping is achieved via propagation through media of given refractive indices that can be engineered to control the optical path of light beams. In this way phase and polarization changes are accumulated through propagation in refractive optical components such as lenses and waveplates. Secondary waves created by diffractive optical components such as holograms propagate in air and interfere in the far-field to form complex patterns. The propagation effect is also used in transformation optics[1,2], which utilizes optical materials structured on a subwavelength scale (metamaterials[3,4]) to produce spatially varying refractive indices that can range from positive to negative. In this way light can be steered in unusual ways, achieving novel phenomena such as negative refraction, perfect lenses and optical cloaking[5–7].

Metasurfaces break our dependence on the propagation effect by introducing abrupt changes of optical properties[8–12]. They can be made of arrays of scatterers or optically thin films. In the former case abrupt and controllable changes of optical properties are achieved by engineering the interaction between light and optical scatterers ('optical antennas'[13,14]), which can take a variety of forms such as metallic or dielectric micro/nanoparticles[15,16] and apertures opened in metallic films[17,18]. The essence of such metasurfaces is to use arrays of antennas with subwavelength separation and with spatially varying geometric parameters (for example, antenna shape, size, orientation) to form a spatially varying optical response, which moulds optical wavefronts into shapes that can be designed at will. This is the main difference between such metasurfaces and frequency selective surfaces[19,20], which typically do not have spatial variations of the electromagnetic response. Metasurfaces based on arrays of optical scatterers are conceptually related to reflect-arrays and transmit-arrays demonstrated in the microwave and millimetre-wave frequency range[21,22].

Metasurfaces of a different nature can be created by using optically thin films made of lossy materials (that is, imaginary part of the complex refractive index comparable to the real part). The phase changes on reflection or transmission of light at the boundary between lossy media can be substantially different from 0 or π (refs 10,23). These nontrivial interfacial phase changes enable nanometre-thin films to substantially modify the light spectrum.

Three features distinguish metasurfaces from conventional optical components. First, wavefront shaping is accomplished within a distance much less than the wavelength from the interface after the incident light beam traverses or is reflected by the optically thin metasurface. Large and controllable changes of the optical properties are achieved through scattering by optical antennas arranged in arrays or through reflection/transmission at interfaces between lossy media. Second, metasurfaces based on optical scatterers enable us to engineer the spatial distribution of amplitude, phase and polarization response with subwavelength resolution. Subwavelength resolution of optical wavefronts makes it possible to funnel all incident optical power into a single useful beam while eliminating other diffraction orders (for example, reflect-array metasurfaces in Fig. 1e,g). This circumvents the fundamental limitation of diffractive optical components, which typically produce multiple diffraction orders. For example, Fresnel zone plates have multiple real and virtual focal points, and holograms generate real images in addition to virtual ones[24]. Furthermore the wide range of spatial frequency components provided by metasurfaces with subwavelength resolution enables the control of the optical near-field and meso-field[25,26], a functionality that has not been systematically explored in conventional optical components. Third, metasurfaces allow one to engineer the interaction of nanostructures with not only the electric field but also the magnetic field component of the light waves[27–29]. This makes it possible to control the optical impedance of planar devices: by matching the impedance with that of free space, one can create high-efficiency transmit-arrays with minimum reflection (Fig. 2c–f).

---

[1]Department of Applied Physics and Applied Mathematics, Columbia University, New York, New York 10027, USA, [2]School of Engineering and Applied Sciences, Harvard University, Cambridge, Massachusetts 02138, USA. *e-mail: capasso@seas.harvard.edu; ny2214@columbia.edu

This Review concentrates on recent developments in the concept and applications of metasurfaces. We start by introducing phase jumps and discuss their implication for light propagation (Fig. 1a,b). Our focus is to illustrate a set of distinctive approaches to create metasurfaces. Metasurfaces made of optical scatterers that control propagating waves are presented in Figs 1–4. Metasurfaces based on holograms in the form of structured metallic surfaces that control surface plasmons[30] are presented in Fig. 5. A hologram can be regarded as a continuous pattern of optical scatterers. Metasurfaces based on optically thin films of lossy materials are presented in Fig. 6.

Optical phase jumps

Richard Feynman used the drowning man's dilemma in his *Lectures on Physics* to explain the refraction of light at the interface between two media[31]. Here we use the dilemma to illustrate the implication of phase jumps for the propagation of light. The drowning man's dilemma asks the following question: what is the best route for a lifeguard to reach a drowning man at sea? Because the lifeguard runs faster than he swims ($v_{\text{land}} > v_{\text{sea}}$), he should head for a point on the seashore that extends the running distance in exchange for a shortened swimming distance. The optimal route satisfies the following equation: $\sin\theta_i/v_{\text{land}} - \sin\theta_t/v_{\text{sea}} = 0$ (white

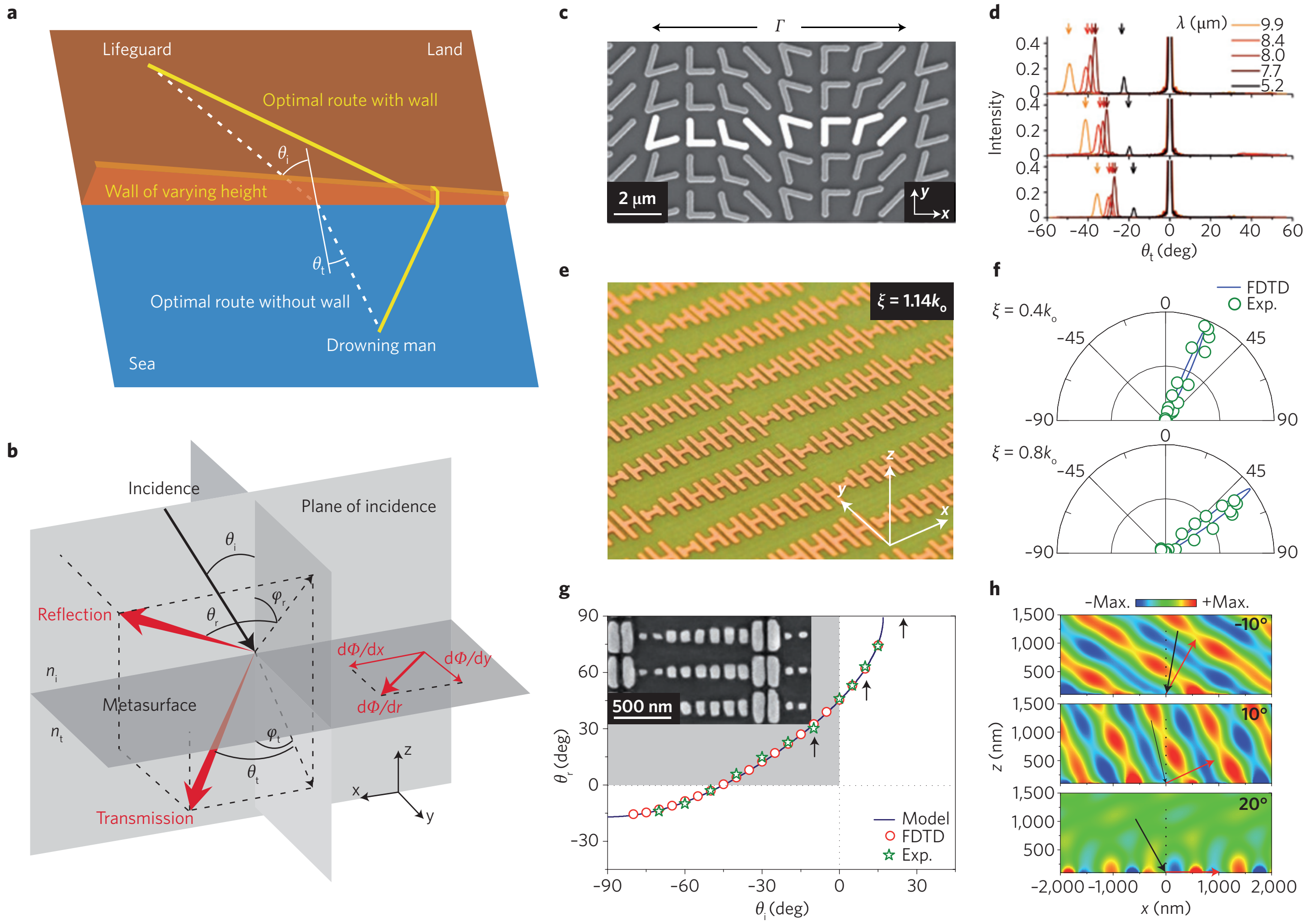

Figure 1 | Generalized laws of refraction and reflection. a, Drowning man's dilemma. A wall with varying height along the seashore will change the optimal route for a lifeguard to reach a drowning man in the sea. Likewise, a gradient of phase jump on the interface between two optical media will change the path of stationary phase according to Fermat's principle, leading to a generalized Snell's law. **b**, A gradient of interfacial phase jump $d\Phi/dr$ provides an effective wavevector along the interface that can bend transmitted and reflected light into arbitrary directions. In particular, the component $d\Phi/dy$ normal to the plane of incidence leads to out-of-plane refraction and reflection. **c**, Scanning electron microscopy (SEM) image of a metasurface consisting of an array of V-shaped gold optical antennas fabricated on a silicon wafer. The metasurface introduces a constant gradient of phase jump along the interface. The unit cell of the metasurface is highlighted and $\Gamma = 11$ μm. **d**, Experimental far-field intensity profiles showing the ordinary and anomalous refraction generated by metasurfaces like the one shown in **c** and with different interfacial phase gradients. The upper, middle and lower panels correspond to $\Gamma = 13$, 15 and 17 μm, respectively. The incident beam impinges normal to the metasurfaces. The far-field profiles are normalized with respect to the intensity of the ordinary beams located at $\theta_t = 0°$. The arrows indicate the calculated angular positions of the anomalous refraction according to $\theta_t = -\arcsin(\lambda/\Gamma)$. **e**, Photograph of a fabricated microwave reflect-array consisting of H-antennas separated from a metallic back plane by a dielectric spacer. The reflect-array introduces an interfacial phase gradient $\xi = 1.14k_o$, where k_o is the wavevector of the incident beam corresponding to a 2-cm wavelength. **f**, Measured and simulated far-field intensity profiles for a microwave reflect-array corresponding to $\xi = 0.4k_o$ and $0.8k_o$. The solid blue lines represent calculations by finite-difference time-domain (FDTD) simulations. **g**, Anomalous reflections at different incident angles for a near-infrared reflect-array consisting of Au patch antennas separated from a gold back plane by a MgF_2 spacer with subwavelength thickness. Note the existence of critical angle of incidence above which there is no reflected wave, consistent with the generalized law of reflection, equation (1). The grey box corresponds to negative reflection. Inset is an SEM image of part of the reflect-array. **h**, Simulated optical fields at different incident angles indicated by the arrows in **g**. The red and black arrows represent the direction of the incident and reflected light, respectively. Figures reproduced with permission from: **b–d**, ref. 12, © 2013 IEEE; **e**,**f**, ref. 38, © 2012 NPG; **g**,**h**, ref. 37, © 2012 ACS.

dashed curve in Fig. 1a). The equation has the same form of Snell's law $\sin\theta_i/v_i - \sin\theta_t/v_t = 0$, where v_i and v_t are, respectively, the phase velocity of light in the media before and after the light beam traverses the interface.

A constant gradient of phase jump on an optical interface is analogous to a wall of linearly varying height along the seashore (Fig. 1a). In planning the optimal route, the lifeguard has to consider the time to climb up and down the wall and decide the best spot to do it. This will necessarily result in an optimal route (yellow solid curve in Fig. 1a) different from the one in the absence of the wall. The optimal route for the lifeguard corresponds to the minimum travelling time, or more rigorously stated is stationary in travelling time with respect to small variations of the route. Similarly, the actual optical path in the presence of phase jumps should be stationary in the total accumulated optical phase. This law of stationary phase has been used to derive the following generalized laws governing the propagation of light[8,32]:

$$\begin{cases} n_t \sin(\theta_t) - n_i \sin(\theta_i) = \dfrac{1}{k_o}\dfrac{d\Phi}{dx} \\ \cos(\theta_t)\sin(\varphi_t) = \dfrac{1}{n_t k_o}\dfrac{d\Phi}{dy} \end{cases} \qquad \text{Generalized law of refraction}$$

$$\begin{cases} \sin(\theta_r) - \sin(\theta_i) = \dfrac{1}{n_i k_o}\dfrac{d\Phi}{dx} \\ \cos(\theta_r)\sin(\varphi_r) = \dfrac{1}{n_r k_o}\dfrac{d\Phi}{dy} \end{cases} \qquad \text{Generalized law of reflection} \tag{1}$$

where the definition of angles are shown in Fig. 1b, $d\Phi/dx$ and $d\Phi/dy$ are, respectively, the components of the phase gradient parallel and perpendicular to the plane of incidence, n_i and n_t are the refractive indices of media on the incident and on the transmission side of the metasurface, respectively and k_o is the magnitude of the free space wavevector. The interfacial phase gradient provides an effective wavevector along the interface that is imparted to the transmitted and reflected photons and the generalized laws can also be derived by considering the conservation of wavevector along the interface. These generalized laws indicate that the transmitted and reflected light beams can be bent into arbitrary directions in their respective half space, depending on the direction and magnitude of the interfacial phase gradient, as well as the refractive indices of the surrounding optical media.

To experimentally demonstrate the generalized laws, one has to devise miniature scatterers that are able to controllably change the phase of the scattered waves and to place such scatterers into an array, forming an artificial interface. The scattering amplitudes should be the same for all scatterers and the spacing between neighbouring scatterers in the array should be much less than the wavelength. These conditions ensure that the superposition of spherical waves emanating from the scatterers gives rise to refracted and reflected waves with planar wavefronts, following Huygens's principle.

Metasurfaces based on optical scatterers

One approach to design the phase response of scatterers is to use antenna dispersion. When a beam of light impinges on a metallic optical antenna, the optical energy is coupled into surface electromagnetic waves propagating back and forth along its surface. These are accompanied by charge oscillations inside the antenna. These coupled surface wave and charge oscillations are known as surface plasmons. Abrupt phase changes over the scale of the free-space wavelength (phase 'jumps') in the direction of the incident light are the result of the strong interaction between light and the localized surface plasmons. For a fixed incident wavelength, antenna resonance occurs when the antenna length $L_{res} \approx \lambda/2$, where λ is the surface plasmon wavelength that accounts for dispersion in the metal; under this condition the incident optical field is in phase with the excited antenna current. When the antenna length is smaller or larger than L_{res}, the current leads or lags the driving field. Therefore, by choosing different antenna lengths one is able to control the phase of the antenna current and thereby the phase of the scattered waves because the scattered light originates from the radiation of the oscillating antenna current. The tuning range of phase is up to π if a single antenna resonance is involved. Multiple independent resonances, coupled antenna resonances or geometric effects (see discussion of the Pancharatnam–Berry phase associated with Fig. 4) are able to extend the phase response to cover the entire 2π range, which is necessary for a complete control of the wavefront. For example, in Fig. 1c the unit cell of the metasurface consisting of eight antennas produces a phase shift of the scattered light that increases from 0 to $7\pi/4$ in steps of $\pi/4$ from one end to the other of the unit cell.

Generalized optical laws were first demonstrated by using V-shaped optical antennas in the mid-infrared spectral range[8] (Fig. 1c,d) and later confirmed in the near-infrared[33]. Such optically anisotropic antennas support two plasmonic eigenmodes with different resonant properties. The geometry and orientation of antennas in the array are properly chosen so that for a normally incident field polarized along a direction oriented at an angle α from the x axis (Fig. 1c), the component of the scattered field polarized along the $90^\circ - \alpha$ direction has an incremental phase of $\pi/4$ between neighbouring V-antennas[27]. The amplitude of the $90^\circ - \alpha$-polarized component is by design uniform across the antenna array and the antenna spacing is between one tenth and one fifth of the free space wavelength. As a result the metasurface in Fig. 1c creates anomalously refracted and reflected beams satisfying the generalized optical laws. The metasurface is broadband: anomalous refraction and reflection are observed and negligible spurious beams and optical background are detected over a wide wavelength range (Fig. 1d). The reasons behind the broadband performance are the following: First, antenna resonances in general have a low quality factor due to high radiation losses; second, the two eigenmodes supported by the V-antennas form a broad effective resonance over which the scattering efficiency is nearly constant and the phase response is approximately linear[34,35]. It is worth noting that the suppression of certain diffraction orders is a characteristic of blazed gratings. Our gradient phased metasurfaces can be regarded functionally as novel blazed gratings[36] but with new important features: the use of phase jumps means easier fabrication and leads to the broadband performance of flat optical components.

The generalized law of reflection has also been demonstrated by using reflect-arrays[37–39], which consist of metallic antennas separated from a back metallic plane by a thin layer of insulator (Fig. 1e–h). The design in Fig. 1e is based on H-shaped antennas for microwaves and the design in Fig. 1g is based on patch antennas working in the near-infrared. Birefringent reflect-array metasurfaces that steer incident light into different directions according to its polarization state have been demonstrated in simulations[39]. The essence of reflect-arrays is to use antennas coupled with their dipolar images in the back plane to achieve a phase coverage of 2π. This approach has the advantage that the antenna scattering efficiency is significantly higher than that of the single-layered design in Fig. 1c (for example, 80% versus 20% in reflectivity) because transmission is suppressed by the back plane. An additional advantage is that the polarization of the reflected light is the same as that of the incident light. Figure 1h shows three regimes of operation for the reflect-array metasurface: negative angle of reflection (upper panel), angle of incidence and angle of reflection both positive but not equal to each other (middle panel), and coupling of incident light directly into evanescent

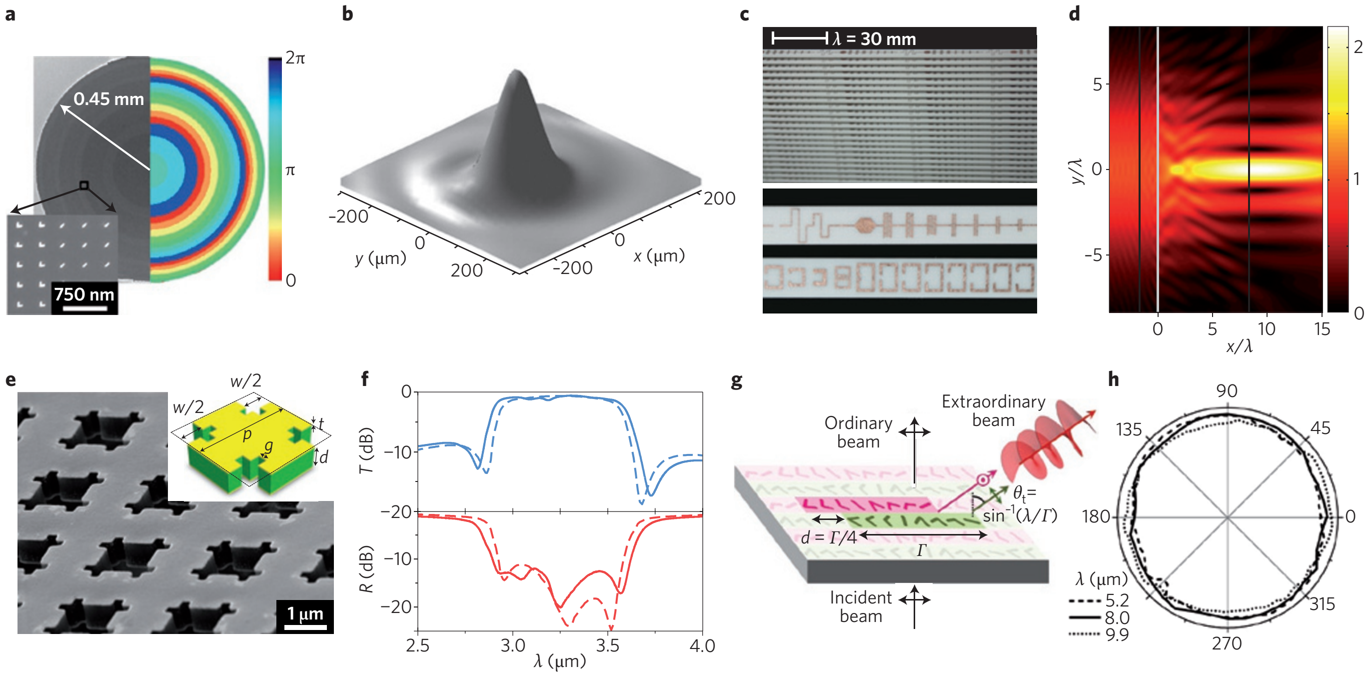

Figure 2 | Planar devices based on metasurfaces. a, Left: SEM image of a fabricated planar lens with 3-cm focal length consists of an array of V-antennas. Right: Phase profile of the lens discretized according to the phase responses of eight constituent antennas. Inset: Zoom-in view of fabricated antennas. The antenna array has a square lattice with a lattice constant of 750 nm. **b**, Measured intensity distribution of the lens in panel **a** on the focal plane. **c**, Top: Photograph of a fabricated microwave metasurface that can redirect an incident beam with nearly 100% efficiency into a refracted beam. It is made of a stack of identical circuit board stripes, the top and bottom sides of which are printed with copper traces. Bottom: One unit cell of the metasurface consists of capacitively and inductively loaded traces to realize desired electric sheet reactance (on the top side of each stripe) and capacitively loaded loops to realize desired magnetic sheet reactance (on the bottom side of each stripe). **d**, Simulation of the electric field magnitude distribution around a Gaussian-to-Bessel beam transformer (located at $x = 0$), which can be realized by the microwave metasurface. **e**, SEM image of a portion of the freestanding nanofabricated fishnet metasurface that functions as a broadband band pass filter. The inset shows a schematic of the unit cell of the metasurface. **f**, Simulated (solid lines) and measured (dashed lines) transmission (upper panel) and reflection (lower panel) spectra of the fishnet metasurface with normally incident excitation showing broadband, close-to-unity transmission from 3.0 μm to 3.5 μm. **g**, Schematic showing a broadband, background-free metasurface quarter-wave plate. The unit cell consists of two subunits (pink and green) each containing eight gold V-antennas. On excitation by linearly polarized incident light, the subunits generate two co-propagating waves with equal amplitudes, orthogonal linear polarizations, and a π/2 phase difference (when offset $d = \Gamma/4$), which produce a circularly polarized extraordinary beam that bends away from the surface normal. **h**, State-of-polarization analysis for the extraordinary beam showing a high degree of circular polarization at $\lambda = 5.2$, 8 and 9.9 μm. The measurements are performed by rotating a linear polarizer in front of a detector and measuring the transmitted power. Figures reproduced with permission from: **a**,**b**, ref. 42, © 2012 ACS; **c**,**d**, ref. 29, © 2013 APS; **e**,**f**, ref. 27, © 2013 NPG; **g**,**h**, ref. 34, © 2012 ACS.

waves on the metasurface (bottom panel). Note that microwave active phased-array antenna is a well-established technology but has substantial differences. The phase of the antennas is typically controlled by phase delay circuits and antenna spacings are usually not subwavelength[40,41].

Figure 2 shows a few planar devices based on metasurfaces. To realize flat lenses, a metasurface should impose a phase profile

$$\varphi_L(x,y) = \frac{2\pi}{\lambda}\left(\sqrt{x^2+y^2+f^2}-f\right) \qquad (2)$$

to mould incident planar wavefronts into spherical ones, which converge at a distance f from the lenses. The optical wavefronts in transmission or reflection remain spherical as long as the incident plane wave impinges normal to the flat lenses. It is therefore straightforward to achieve high numerical-aperture (NA) focusing without spherical aberration. Flat lenses at telecom wavelength have been experimentally demonstrated using V-shaped antennas (Fig. 2a,b)[42]. V-shaped aperture antennas have a similar optical response to their complementary structures of V-antennas according to Babinet's principle; they have been used to create flat lens to focus visible light[43]. The efficiency of the flat lens reported in ref. 42 is small (that is, ~1% of the incident optical power is focused) because only a single layer of scatterers was used, the surface filling factor is small, and only the cross-polarized component of the scattered light is focused. A flat lens design at telecom wavelength with potentially much higher efficiency has been demonstrated in simulations[44]. The design uses concentric loop antennas placed on both sides of a substrate to enhance scattering efficiency and to increase the range of phase coverage. Flat lenses working in the near-infrared with high efficiency have been demonstrated experimentally by using reflect-arrays of patch antennas[45]. Note that except for spherical aberration, monochromatic aberrations are still present in the above demonstrated flat lenses. For example, when incident light is not perpendicular to the lenses, the transmitted or reflected wavefront is no longer spherical because its phase distribution is that as described by equation (2) plus a linear phase distribution introduced by the non-normal incidence angle. Theoretical analysis shows that this aberration, known as coma, can be greatly reduced compared with conventional bulk spherical lenses by building the flat lens on a curved substrate (F. Aieta, personal communication). Flat lenses also have chromatic aberration and one can design antennas with multiple resonances to eliminate it by engineering their dispersion.

To boost the efficiency of metasurfaces in controlling the transmitted light, one has to match its impedance with that of free space. Complete elimination of reflection can be realized by controlling the surface electric and magnetic polarizabilities, α_e and α_m, of the metasurfaces so that[29]

$$\sqrt{\alpha_m / \alpha_e} = \eta_o \tag{3}$$

where η_o is the free space impedance. The effective electric and magnetic surface currents, which are proportional to α_e and α_m, respectively, change the boundary conditions at the metasurface and lead to the new scattered wavefronts. The complex transmission coefficient of the metasurface is[29]

$$T = \frac{2 - i\omega\alpha_e\eta}{2 + i\omega\alpha_e\eta}$$

where ω is the angular frequency. So as long as α_e is real, one can change its value (and correspondingly α_m according to equation (3)) to provide complete phase coverage from $-\pi$ to $+\pi$. The above design concept has been implemented in the microwave spectral region by using spatially varying copper traces supporting both electric and magnetic polarization currents[29] (Fig. 2c). Transmission efficiency of 86% was demonstrated in a beam deflector and simulations show that complex flat components such as a Gaussian-to-Bessel beam transformer with high efficiency can be realized (Fig. 2d). Although the demonstrations are in the microwave regime, the concepts can be adapted to optics. Another metasurface impedance matched to free space and able to fully control the phase of the transmitted light was proposed in a recent paper[28]. It is designed based on optical nanocircuit concepts and comprises three planarized arrays stacked together. The building blocks of the array are subwavelength components made of metallic and dielectric materials with different filling ratios and function as inductors and capacitors at optical frequencies. A beam deflector and a flat lens with high transmission efficiency were demonstrated in simulations by engineering the effective surface impedance of the metasurface via tuning of the filling ratios.

The flexibility in engineering the dispersion of metasurfaces was also demonstrated in a mid-infrared band-pass filter[27] (Fig. 2e,f). In this case the effective permittivity and permeability, ε_{eff} and μ_{eff}, of the thin metamaterials (thickness ~1/6 free space wavelength) are designed to balance each other so that over a wide spectral range the effective impedance $\eta_{\text{eff}} = \sqrt{\mu_{\text{eff}}/\varepsilon_{\text{eff}}}$ is matched to that of free space, leading to a transmission coefficient close to unity. Outside of this pass-band, ε_{eff} and μ_{eff} are imbalanced to produce an effective impedance that blocks the transmission of waves. Control of the dispersion of the thin metamaterial is achieved by engineering the plasma frequency, the electric/magnetic resonance frequencies and the damping factors of its constituent elements.

Figure 2g,h shows a broadband metasurface quarter-wave plate[34]. Here a combination of antenna dispersion and rotation of the antenna axes are used to control both the phase and polarization response of the metasurface, so that when a linearly polarized beam normally impinges on the metasurface, it creates a circularly polarized beam propagating away from the surface normal. The metasurface quarter-wave plate has been demonstrated experimentally to generate a high degree of circular polarization (>0.97) from λ = 5 to 10 μm. The key underlying this broadband performance is that the anisotropic antennas used in this case support

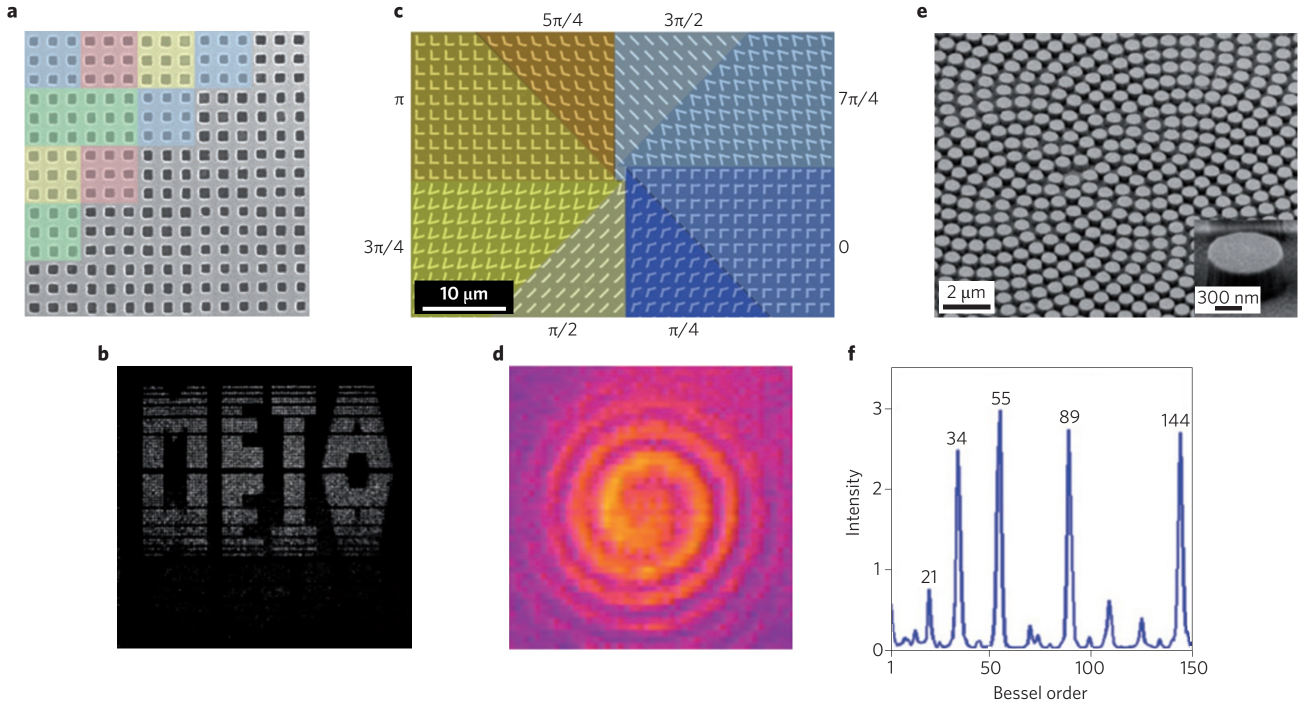

Figure 3 | Complex wavefront shaping based on metasurfaces. a, SEM image of part of a metasurface hologram made of aperture antennas. Different colours represent pixels with distinctive transmission coefficients. Size of image, 9 μm × 9 μm. **b**, Transmitted light intensity of the metasurface in panel **a** recorded in the far-field. Incident wavelength is 905 nm. **c**, SEM image of the central region of a mid-infrared metasurface phase plate that is able to generate optical vortex beams. The plate comprises eight regions, each occupied by one V-antenna type. The antennas are arranged to create a phase shift that varies azimuthally from 0 to 2π, thus producing a helicoidal scattered wavefront corresponding to an orbital angular momentum $L = 1$. **d**, Spiral interferogram created by the interference between a vortex beam created by the plate in panel **c** and a co-propagating Gaussian beam. The size of the interferogram is about 30 mm × 30 mm. **e**, SEM image of a spiral pillar array fabricated in Er-doped Si-rich silicon nitride. The structure functions as a binary hologram. The inset is an SEM image of a single pillar. **f**, Calculation showing that Er photoluminescence from the structure in panel **e** contains several discrete vortex beams with L corresponding to 5 consecutive Fibonacci numbers (that is, 21, 34, 55, 89 and 144). Figures reproduced with permission from: **a**,**b**, ref. 17, © 2012 Wiley; **e**,**f**, ref. 49, © 2012 AIP.

two resonances that effectively broaden the spectral range over which the scattering efficiency is high and over which the phase response is approximately linear as a function of wavelength.

Figure 3 shows complex wavefront shaping based on metasurfaces. Figure 3a shows a metasurface consisting of arrays of aperture antennas that produce a spatially varying transmission coefficient[17]. By utilizing the dispersion of aperture antennas, the metasurface was designed to operate as two distinctive holograms at two different wavelengths, λ_1 = 905 nm, λ_2 = 1,385 nm. It creates a word 'META' in the far-field at λ_1 = 905 nm (Fig. 3b). A different pattern is created in the far-field at λ_2 = 1,385 nm. Figure 3c,d shows a metasurface that generates an optical vortex beam[46], which carries orbital angular momentum (OAM). The vortex beam has cork-screw shaped wavefronts and the Poynting vector of the beam follows a spiral trajectory around the beam axis, giving rise to the OAM[47,48]. The order of orbital angular momentum L is the number of twists of the spiral wavefront along a propagation distance equal to one wavelength. The metasurface is created by assembling an array of V-antennas so that in the azimuthal direction the phase response increases linearly from 0 to 2π. The wavefront of the vortex beam can be revealed by a spiral interferogram produced by the interference between the beam and a co-propagating Gaussian beam (Fig. 3d). Figure 3e shows a 'sunflower' pattern of silicon nitride pillars. The pattern acts like a hologram that can generate in the far-field a superposition of vortex beams with topological charge corresponding to consecutive Fibonacci numbers (Fig. 3f)[49].

In the previous examples, variations in phase or amplitude response are introduced by the dispersion of antenna resonance. For example, a suitable phase distribution at a certain wavelength is created by using an array of antennas with spatially varying geometric parameters. A completely different approach to introducing abrupt phase changes, which are not subject to antenna dispersion, is to use the Pancharatnam–Berry phase[50,51]. The latter is associated with polarization change and can be created by using anisotropic, subwavelength scatterers with identical geometric parameters but with spatially varying orientations. The easiest way to reveal the relation between polarization and phase is to use Jones calculus. One example is shown in Fig. 4a, which demonstrates that an azimuthally polarized optical vortex beam is created when a circularly polarized beam traverses an array of identical apertures oriented with radial symmetry[52].

A slit aperture defined in a metallic film functions like a miniature polarizer: the transmitted light through the aperture has a polarization primarily perpendicular to its long axis. Therefore, one can use the Jones matrix of a polarizer[53]

$$\mathbf{M}_{\text{pol}} = \begin{pmatrix} \cos^2\alpha & \sin\alpha\cos\alpha \\ \sin\alpha\cos\alpha & \sin^2\alpha \end{pmatrix}$$

to represent the aperture; here α is the orientation angle of the slit aperture. The transmitted wave $\mathbf{E}_{\text{T}}^{\text{R/L}}$ through the aperture for right/left circular incident polarization $\mathbf{E}_{\text{I}}^{\text{R/L}}$ is:

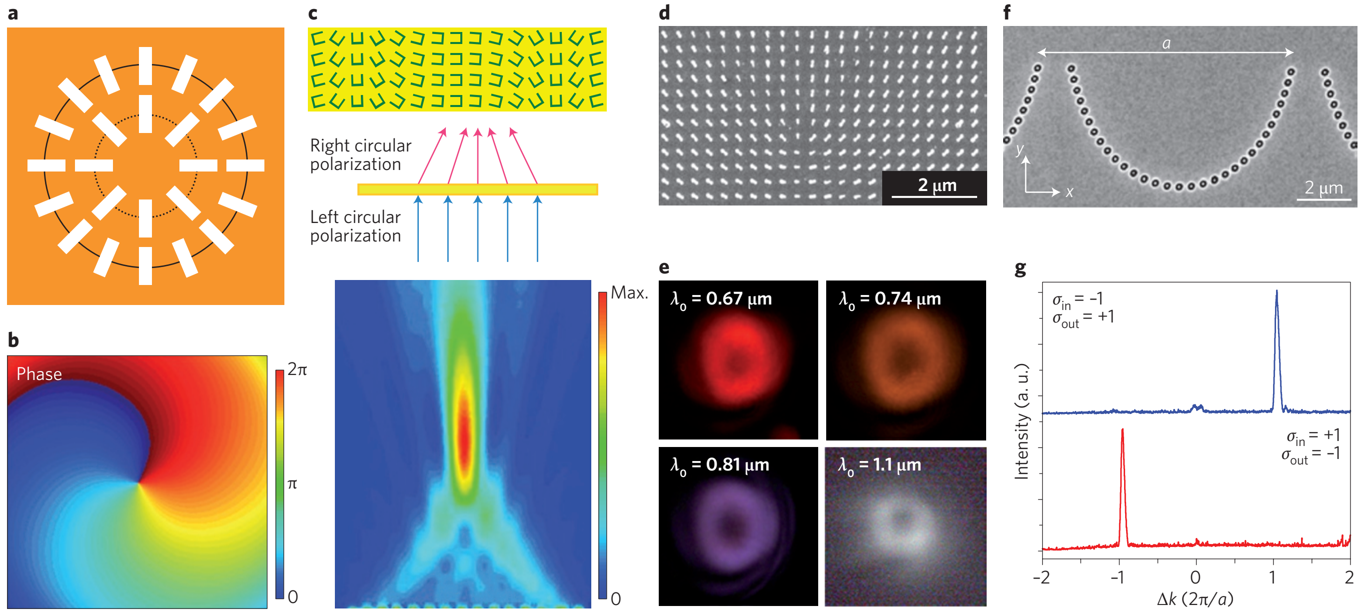

Figure 4 | Variation of the polarization state of light is associated with a geometrical phase change (that is, the Pancharatnam–Berry phase). This property is used to design planar optical components using metasurfaces with spatially varying polarization response. **a**, Geometry of a metasurface composed of rectangular apertures defined in a metal film and arranged into an array with rotational symmetry. **b**, Simulated phase distribution of the azimuthally polarized transmitted field. Incident light is circularly polarized. **c**, Upper panel: Schematic of a planar cylindrical lens consisting of arrays of U-apertures with different orientations. Lower panel: Schematic and simulation showing that the lens focuses the right-handed circularly polarized (RHCP) component of the transmission when the incident light is left-handed circularly polarized (LHCP). **d**, SEM image of a dipolar antenna array designed for generating an optical vortex beam with L = 1 (RHCP incidence/LHCP detection). The antennas have the same geometry but spatially varying orientations. **e**, Measured intensity distribution of vortex beams generated by the metasurface in panel **d** at different wavelengths from 670 to 1,100 nm. As the phase jump originates from polarization changes in the scattered light of the dipolar antennas (not the dispersion of the antennas, which is used in metasurfaces in Figs 1–3) the metasurface can operate over a wide range of wavelengths. **f**, SEM image of an array of coupled coaxial nanoapertures, which form a curved chain whose local orientation is varied linearly along the x axis with a period of a = 9 μm, and a structure length of 135 μm. The local orientation of the curved chain induces local anisotropy in the scattered field, giving rise to a spatial distribution of Pancharatnam–Berry phase equivalent to an interfacial wavevector of $\Delta k_x = -2\sigma\pi/a$, where $\sigma = \pm1$ is the incident spin state (that is, RHCP or LHCP). **g**, Spin-dependent beam deflection observed in experiments using the sample in **f**. Figures reproduced with permission from: **a**,**b**, ref. 52, © 2012 OSA; **c**, ref. 54, © 2012 OSA; **d**,**e**, ref. 56, © 2012 ACS; **f**,**g**, ref. 57, © 2011 ACS.

$$\begin{aligned}E_T^{R/L} &= M_{pol}\cdot E_I^{R/L}\\ &= \begin{pmatrix}\cos^2\alpha & \sin\alpha\cos\alpha\\ \sin\alpha\cos\alpha & \sin^2\alpha\end{pmatrix}\begin{pmatrix}1\\ \mp i\end{pmatrix}\\ &= \exp(\mp i\alpha)\begin{pmatrix}\cos\alpha\\ \sin\alpha\end{pmatrix}\end{aligned}$$

The result indicates that the transmission is linearly polarized along the α-direction and carries an additional Pancharatnam–Berry phase of $\mp\alpha$. Therefore the aperture array shown in Fig. 4a with α ranging from 0 to 2π will imprint a spiral phase distribution to the transmitted wavefront, creating a vortex beam with $L = 1$.

In general, the Jones matrix of an anisotropic scatterer can be written as

$$M_{ani} = R(-\alpha)\begin{pmatrix}t_o & 0\\ 0 & t_e\end{pmatrix}R(\alpha)$$

where t_o and t_e are, respectively, the complex scattering coefficients for incident light linearly polarized along the two axes of the anisotropic scatterer.

$$R(\alpha) = \begin{pmatrix}\cos\alpha & \sin\alpha\\ -\sin\alpha & \cos\alpha\end{pmatrix}$$

is the rotation matrix. The scattered light from the anisotropic scatterer in the forward direction can then be written as[54]:

$$E_T^{R/L} = M_{ani}\cdot E_I^{R/L} = \frac{t_o + t_e}{2}E_I^{R/L} + \frac{t_o - t_e}{2}\exp(\mp i2\alpha)E_I^{L/R}$$

The first term represents circularly polarized scattered waves with the same handedness as the incident light and the second term represents circularly polarized scattered waves with opposite handedness and an additional Pancharatnam–Berry phase of $\mp 2\alpha$. The second component can be selected in experiments by using a quarter-wave plate and a polarizer. Its phase can cover the entire 0–2π range if the anisotropic scatterer is rotated from 0 to 180°. Based on this principle, planar lenses were demonstrated by using identical rod antennas or U-shaped apertures (Fig. 4c) with different orientations[54,55], and a broadband phase plate generating optical vortex beams was demonstrated by using rod antennas (Fig. 4d,e)[56].

Optical anisotropy can also be created by coupled isotropic nanoscatterers. One example is shown in Fig. 4f,g[57]. Here the axis of anisotropy traces an array of coaxial nano-apertures: from one end to the other end of the half-circle pattern (one period of the array) the axis of anisotropy rotates by 180°, creating a constant gradient of Pancharatnam–Berry phase along the x axis.

The metasurfaces in Fig. 4c,d,f work for circularly polarized incident light and control the component of the circularly polarized transmission with the opposite handedness. A major advantage of the approach based on Pancharatnam–Berry phase is ultra-broadband performance: there is no wavefront distortion

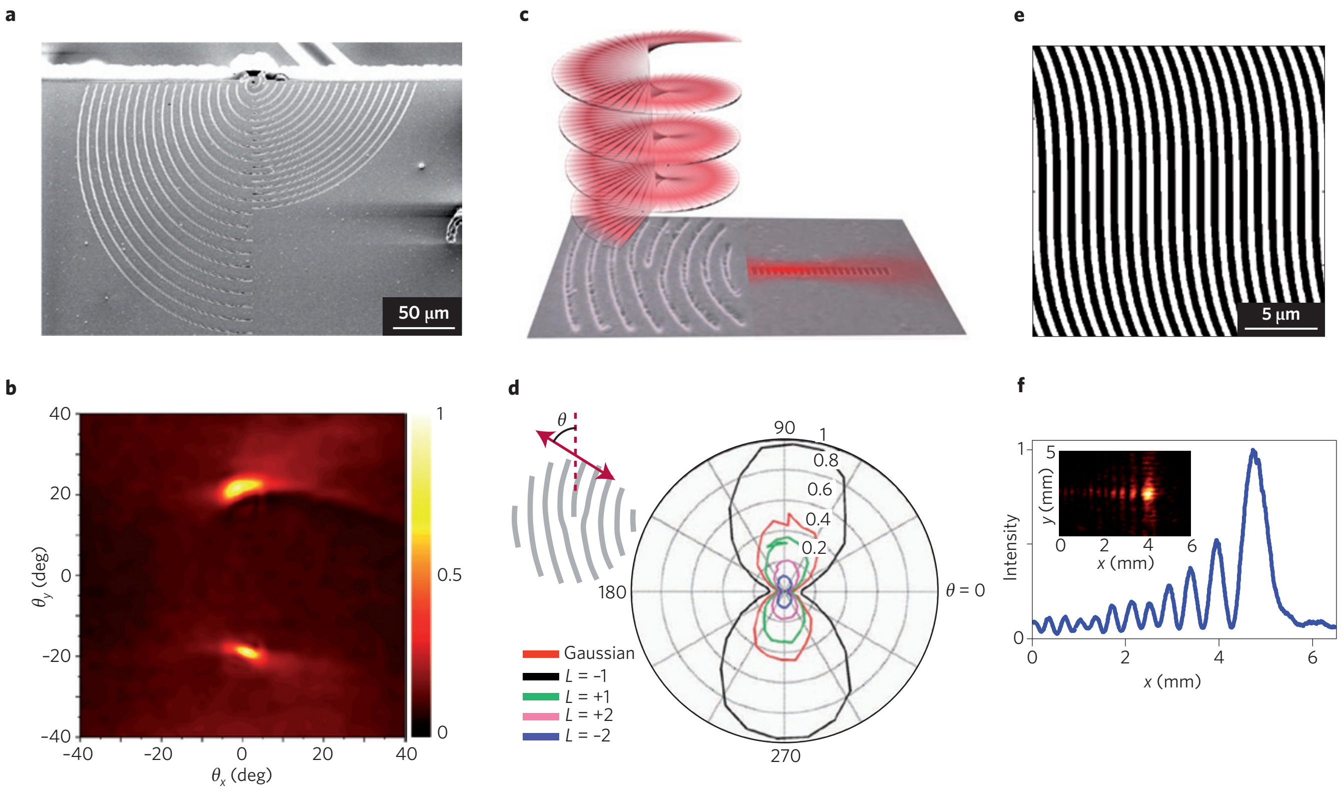

Figure 5 | Hologram-based flat optics. a, SEM image of a plasmonic lens producing two beams and fabricated on the facet of a quantum cascade laser. The lens consists of two sets of elliptical grooves, each creating one beam by scattering surface waves generated from an aperture located at the end of the laser waveguide. **b**, Measured far-field intensity of the device shown in **a**. **c**, A holographic coupler consisting of curved, fork-shaped grooves converts an incident vortex beam with $L = -1$ into a focused surface wave, which is then funnelled into a detector underneath the metal film by an array of subwavelength holes. **d**, Detected photocurrent as a function of the incident polarization for incident beams with different orbital angular momentum. The inset shows the orientation with respect to the grooves of the polarization of the incident electric field, represented by the double headed arrow. **e**, Holographic pattern with a cubic phase modulation $g(x,y) = 1 + \mathrm{sgn}\{\cos(2\pi f_{carrier}x + 75y^3/500^3)\}$, where $1/f_{carrier} = 0.98$ µm is the period of the pattern. **f**, Cross section of an Airy beam generated by scattering surface waves from the cubic holographic pattern. Inset is the measured 2D intensity of the Airy beam in the far-field. Figures reproduced with permission from: **a**,**b**, ref. 60, © 2011 IOP; **d**, ref. 61, © 2012 NPG; **e**,**f**, ref. 62, © 2012 APS.

resulting from antenna dispersion. The operating bandwidth is limited on the long-wavelength side by reduced scattering efficiency and on the short-wavelength side by the requirement that the wavelength has to be at least several times larger than the spacing between scatterers (that is, metasurface regime).

The metasurfaces shown in Figs 1–4 can be regarded as holograms with subwavelength resolution that carry information of the phase, amplitude and polarization of the desired wavefront. A hologram is essentially the interference pattern between a reference beam and the desired beam. The latter is reconstructed when the reference beam impinges on the hologram. One can generalize this principle and create holograms that convert incident reference beams into desired surface waves or couple surface waves back into waves in free space with desired properties[58,59]. Figure 5a shows a plasmonic lens defined on the facet of a mid-infrared quantum cascade laser[60]. The plasmonic lens progressively scatters the optical power of surface plasmons generated from a subwavelength aperture at the end of the laser waveguide into free space, forming collimated beams in the far-field (Fig. 5b). Elliptical plasmonic grooves were used because the interference pattern between a surface wave with circular wavefronts and a plane wave propagating in a direction not perpendicular to the surface is elliptical. Figure 5c shows another binary hologram that allows the detection of optical vortex beams with specific OAM[61]. It works by coupling an incident optical vortex beam with a certain OAM into focused surface plasmons, which are then detected by a photodetector. The interference between a vortex beam perpendicular to a surface and a focused surface plasmon forms a curved fork; therefore a binary curved-fork pattern is used as the hologram. Figure 5e shows a holographic pattern with cubic phase modulation. A metallic surface with grooves based on this pattern was used to convert surface plasmons into Airy beams in free space (Fig. 5f)[62]. The holographic technique was also used at microwave frequencies to create designer impedance surfaces that convert surface currents into far-field radiation with desired properties[63,64]. In particular, tensorial impedance surfaces are able to control the polarization state of the radiation. For example, circularly polarized radiation is generated from a radially distributed surface current.

Metasurfaces based on thin films

In the previous examples spatially inhomogeneous (quasi) two-dimensional (2D) patterns with subwavelength resolution are used to mould optical wavefronts. Figure 6 shows another dimension in the manipulation of light waves by using optically thin, lossy films on lossy substrates. As the amplitudes of partial waves reflected from the thin films are complex quantities, we can plot them in the complex plane as phasors (Fig. 6b). The amplitude and phase of a partial reflected wave are represented by the length and direction of a phasor, respectively. The first phasor r_0 begins at the origin, r_1 begins at the end of r_0, and so on. The total reflectivity is the magnitude-squared of the final value of the phasor trajectory. By properly choosing the materials of the film and the substrate, we can control the phase that light experiences reflecting at the interface between air and the film and at the interface between the film and the substrate, making it possible to engineer the phasor diagram or the reflection spectrum. Because the films have a thickness much smaller than the wavelength of light, an equivalent semi-infinite medium can be defined that has essentially the same reflection spectra as the combined thin-film/substrate structure for various angles of incidence[10]. In this sense, the thin-film/substrate structure can be regarded as a metamaterial with controllable complex refractive indices.

Figure 6a is a schematic illustration of a mid-infrared perfect absorber based on vanadium dioxide (VO_2) thin films[23]. VO_2 undergoes an insulator-to-metal transition around $T_c = 340$ K (ref. 65). In the vicinity of the phase transition, the percolation of metallic nanostructures in an insulating matrix (Fig. 6c) leads to a tunable complex effective refractive index $n_1 + ik_1$. In this sense VO_2 is a tunable metamaterial. The sapphire substrate is a lossy material in the mid-infrared with $n_2 + ik_2$. Perfect absorption is reached for a 180-nm-thick VO_2 film on sapphire at $T = 343$ K and at $\lambda = 11.6$ μm when $n_1 + ik_1 \approx 4 + 3.5i$ and $n_2 + ik_2 \approx 0.1 + 0.8i$ (Fig. 6d). Under this condition the phase of the first partial wave is close to π so r_0 is pointing to the left (Fig. 6b). The phasor trajectory makes a sharp turn after r_0 because of the near-zero phase shift that light experiences reflecting from the VO_2/sapphire interface. As a result r_1 partially cancels r_0. The net effect is that a film 65 times thinner than the wavelength of the incident light can create perfect absorption (that is, 0.25% reflectivity) when light waves bounce a few times inside the film (Fig. 6b). By tuning the sample temperature, one can easily switch the film between its absorbent and non-absorbent states, which implies possible applications in tunable filters, bolometers and spectroscopy devices. Figure 6e shows another example where tiny variations in the thickness of germanium films (~10 layers of germanium atoms) on a gold substrate lead to drastically different colours[10]. Physically, the phase shift of light reflection from a germanium/gold interface is substantially different from π, the value for reflection from an ideal metal, so that much thinner germanium films are needed to observe interference effects. Recently strong-to-perfect absorption and selective thermal emission across a wide range of mid-infrared wavelengths (5–12 μm) using a two-layer system consisting of heavily doped silicon and a thin germanium dielectric layer has been realized[66]. Figure 6f shows a schematic of a water-splitting cell based on thin films of α-Fe_2O_3. As much as 70% of the solar photons of energy above the bandgap energy of α-Fe_2O_3 (2.1 eV) can be absorbed by the cell and high photon fluxes are concentrated close to the surface of the cell, which is critical for the water-splitting reaction[67]. These studies confirm that interference effects in optically thin and lossy films can be observed in a variety of technologically important material systems and exploited in low-cost device applications.

Applications and outlook

Wavefront shaping through local control of phase, amplitude and polarization on an optically thin plane will lead to a new class of flat optical components in the areas of integrated optics, flat displays, energy harvesting and mid-infrared photonics, with increased performance and functionality. In this respect it is important to note that integrated circuits manufacturing are based on planar technology that tremendously simplifies fabrication compared with making 3D structures. A large body of research on photonic crystals and metamaterials has concentrated on 3D structures that although physically interesting in our opinion will only find niche applications in technology[68–72]. Flat optical components based on metasurfaces are naturally better suited for large-scale applications because the fabrication complexity is greatly reduced. A variety of lithographic techniques for large-scale patterning of planar structures are available ranging from deep UV lithography, to nanoimprint lithography and soft lithography.

Metasurfaces are functionally similar to diffractive optical components: both technologies shape light beams for different applications by using a planar architecture. However, metasurfaces rely on a toolset of designer structures different from those used in diffractive optics. These new structures provide such unprecedented flexibility that one can engineer the interaction between metasurfaces and the electric as well as the magnetic field components of light independently[27–29] (Fig. 2c–f), which leads to complete control of not only the phase, amplitude and polarization response but also of the impedance response of the metasurfaces. This control is not limited to a single wavelength but can be extended to

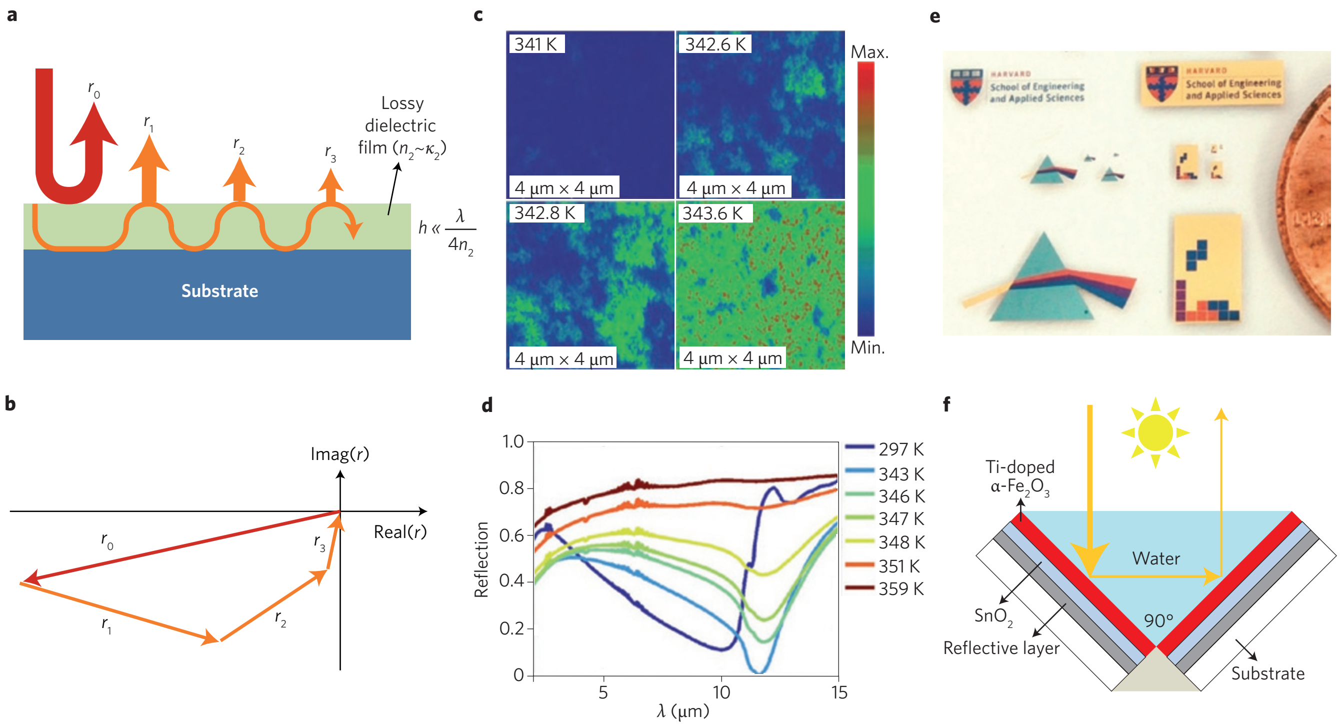

Figure 6 | Thin-film flat optics. **a**, Reflection process from a highly absorbing ultrathin film on a lossy substrate. **b**, Phasor diagram demonstrating that a perfect absorption condition is achievable if the complex refractive indices of the film and the substrate are properly chosen so that the phasor trajectory returns to the origin. **c**, Near-field scanning optical microscopy images showing the percolation process in a VO_2 film. The images were obtained by recording scattered near-field amplitude at $\lambda = 10.75$ μm in the vicinity of the insulator-to-metal phase transition temperature (~67 °C). Metallic regions have large scattering amplitude. **d**, Experimental reflection spectra of a sample consisting of a sapphire substrate coated with 180 nm of VO_2 at temperatures from 297 K to 359 K. Maximum absorption (reflectivity ~0.0025) is reached at $\lambda = 11.6$ μm at 343 K. **e**, Photograph of colour images generated using multistep patterning of ultrathin germanium films. Five steps of photolithography with alignment are used to selectively deposit an optically thick layer of Au on a glass slide, followed by Ge layers of 7, 11, 15 or 25 nm, yielding light pink, purple, dark blue and light blue colours, respectively. **f**, Schematic illustration of a water-splitting cell comprising Ti-doped α-Fe_2O_3 films, ultrathin SnO_2 layers, reflective layers (alloy with 90 at.% silver and 10 at.% gold) and glass substrates. In one demonstrated device, the thickness of α-Fe_2O_3 films, SnO_2 layers and reflective layers is ~20 nm, ~5 nm and ~1.2 μm, respectively. The SnO_2 layers serve as selective electron-transport layers that block the injection of holes from the α-Fe_2O_3 films to the substrates, so most of the photogenerated holes can reach the surface and oxidize water before recombination takes place. Figures reproduced with permission from: **a**,**b**, ref. 23, © 2012 AIP; **c**, ref. 65, © 2007 AAAS; **d**, ref. 23, © 2012 AIP; **e**, ref. 10, © 2013 NPG; **f**, ref. 67, © 2013 NPG.

a certain spectral range by suitable dispersion engineering of the constituent elements of the metasurfaces. These advantageous features go well beyond the capabilities of conventional diffractive optical components, which do not specifically consider surface impedance engineering and typically have little control of chromatic dispersion. As such it is likely that new functionalities will emerge from flat optics based on metasurfaces, not possible with conventional diffractive optics.

From a strictly technological point of view many of the metasurfaces described in this Review represent a much simpler way to implement diffractive optics than with conventional techniques. From the examples discussed it is clear that with metasurfaces one can create arbitrary analogue phase, amplitude and/or polarization profiles using a single digital mask and a single lithography process. In this case, the metasurface can be as thin as the skin depth of light in a metal (for example, 25 nm for gold in the mid-infrared). A multilayered architecture is in general needed for metasurfaces that not only control phase, amplitude and/or polarization of the wavefronts but are also impedance matched to free space. The fabrication therefore will be more complex but still should be feasible.

Flat lenses and other optical components based on a variety of mechanisms have been demonstrated to shape the scattered wavefront, including spatial light modulators, binary phase gratings, microelectromechanical systems (MEMS), surface relief modulation and effective index modulation[73]. The complexity of fabricating these planar structures varies by a large degree. Pure phase modulation is typically realized by liquid-crystal spatial light modulators[74], binary phase gratings[75] and MEMS micromirror arrays[76,77]. Complex phase-amplitude modulation can be achieved by multilayered, metal–dielectric diffractive structures[78]. Surface relief modulation is realized by several techniques including variable-dose electron-beam lithography[79], laser ablation[80], direct laser writing in photoresist[81] and photolithography based on grey-scale masks[82,83]. Advanced techniques involving nonlinear optical light–matter interactions such as two-photon polymerization[84,85] and metal-ion photoreduction[86] have the promise to create sophisticated planar or 3D structures. Index modulation can implement quasi-analogue phase profiles and has been demonstrated using electron-beam irradiation[87] and effective media with subwavelength features[88–92]. Except for intensity modulation that is based on diffractive masks made of alternating absorbing/reflective and transmissive areas, essentially all other diffractive components still rely on propagation of light through structured thin slabs to change the optical phase, which implies: (a) they cannot be orders of magnitude thinner than the free space wavelength; (b) they can hardly be broadband.

Although work on metalenses is in its infancy it offers in the long run major opportunities if broadband, aberration-free, high NA lenses can be realized. This would dramatically reduce the complexity of currently used objectives that employ multiple lenses for aberration correction. Myriad of applications would benefit, from ultrathin smart phones to photography and optical instrumentations. Flat optics technology is ideally suited for the facet of optical fibres to which flat lenses could be transferred using soft-lithography techniques[93], which would open up many opportunities in biomedical imaging.

Refractory optics in the mid-infrared is far less developed than at shorter wavelengths due to limited availability of suitable materials and not sufficiently advanced fabrication technology. Our calculations show that mid-infrared high NA focusing reflect-arrays with high efficiency in excess of 90% at specific wavelengths can be realized. In particular the realization of high NA lenses free of chromatic aberrations in the 3–5 μm and 8–13 μm spectral regions would have major impact on imaging systems such as infrared cameras. Important applications in the mid-infrared that utilize metasurfaces based on designer scatterers are thermal emitters with engineered emissivity that can be used as beacons for identification and targeting[66,94]. Metasurfaces based on nanometre-thick lossy films of the type discussed in this Review have significant potential application in detectors and even solar cells.

The arrays of subwavelength-spaced optical scatterers used to design many metasurfaces can be implemented using optical antennas, dielectric resonators, nanocrystals, quantum dots and so on. Relying on phase jumps in optically thin structures to shape the wavefront of light beams allows one to transfer the functionality of transmit-arrays and reflect-arrays from the microwave to the optical spectral region, opening up a large space for applications. Particularly exciting is the frontier of reconfigurable flat optics. This can be done by building the arrays on materials where the refractive index can be significantly changed using external parameters such as the voltage[95–102], temperature[23,65,103], light[104,105] and magnetic field[106]. Graphene, where electric field effects can produce large variations in the optical conductivity[96–102], is a good candidate, along with phase-change materials such as vanadium dioxide and others that undergo near room temperature the insulator-to-metal transition[65]. Building metasurfaces on stretchable materials such as elastomers also offers fresh opportunities in reconfigurable photonics[107]. We ultimately envisage optical phased arrays[108] with fast (nanosecond timescale) wavefront tuning and possibly beam steering, which will open a major space for military and civilian applications. There is still room for optimizing the performance of flat optics and exploring its new functionalities. We see great potential for flat-optics-based components such as reduction in system size and weight, elimination of difficult-to-process refractory materials in spectral regions such as the mid-infrared, increased design freedom in correcting aberrations, achieving high scattering efficiency and broadband performance by impedance matching, and reconfigurability.

Received 20 April 2013; accepted 14 November 2013; published online 23 January 2014

References

1. Pendry, J. B., Schurig, D. & Smith, D. R. Controlling electromagnetic fields. *Science* **312,** 1780–1782 (2006).
2. Leonhardt, U. Optical conformal mapping. *Science* **312,** 1777–1780 (2006).
3. Cai, W. & Shalaev, V. *Optical Metamaterials: Fundamentals and Applications* (Springer, 2009).
4. Engheta, N. & Ziolkowski, R. W. *Metamaterials: Physics and Engineering Explorations* (Wiley-IEEE, 2006).
5. Shelby, R. A., Smith, D. R. & Shultz, S. Experimental verification of a negative index of refraction. *Science* **292,** 77–79 (2001).
6. Fang, N., Lee, H., Sun, C. & Zhang, X. Sub-diffraction-limited optical imaging with a silver superlens. *Science* **308,** 534–537 (2005).
7. Schurig, D. *et al.* Metamaterial electromagnetic cloak at microwave frequencies. *Science* **314,** 977–980 (2006).
8. Yu, N. *et al.* Light propagation with phase discontinuities: Generalized laws of reflection and refraction. *Science* **334,** 333–337 (2011).
9. Holloway, C. L. *et al.* An overview of the theory and applications of metasurfaces: The two dimensional equivalents of metamaterials. *IEEE Antennas Propagat. Mag.* **54,** 10–35 (2012).
10. Kats, M. A., Blanchard, R., Patrice, G. & Capasso, F. Nanometre optical coatings based on strong interference effects in highly absorbing media. *Nature Mater.* **12,** 20–24 (2013).
11. Kildishev, A. V., Boltasseva, A. & Shalaev, V. M. Planar photonics with metasurfaces. *Science* **339,** 1232009 (2013).
12. Yu, N. *et al.* Flat optics: Controlling wavefronts with optical antenna metasurfaces. *IEEE J. Sel. Top. Quant. Electron.* **19,** 4700423 (2013).
13. Bharadwaj, P., Deutsch, B. & Novotny, L. Optical antennas. *Adv. Opt. Photon.* **1,** 438–483 (2009).
14. Novotny, L. & van Hulst, N. Antennas for light. *Nature Photon.* **5,** 83–90 (2011).
15. Svirko, Y., Zheludev, N. & Osipov, M. Layered chiral metallic microstructures with inductive coupling. *Appl. Phys. Lett.* **78,** 498–500 (2001).
16. Zou, L. *et al.* Dielectric resonator nanoantennas at visible frequencies. *Opt. Express* **21,** 1344–1352 (2013).
17. Walther, B. *et al.* Spatial and spectral light shaping with metamaterials. *Adv Mater*. **24,** 6300–6304 (2012).
18. Lin, J. *et al.* Polarization-controlled tunable directional coupling of surface plasmon polaritons. *Science* **340,** 331–334 (2013).
19. Munk, B. A. *Frequency Selective Surfaces: Theory and Design* (Wiley, 2000).
20. Wu. T. K. *Frequency Selective Surface and Grid Array* (Wiley, 1995).
21. Pozar, D. M., Targonski, S. D. & Syrigos, H. D. Design of millimeter wave microstrip reflectarrays. *IEEE Trans. Antenna Propag.* **45,** 287–295 (1997).
22. Gagnon, N., Petosa, A. & McNamara, D. A. Research and development on phase-shifting surfaces. *IEEE Antennas Propag. Mag.* **55,** 29–48 (2013).
23. Kats, M. A. *et al.* Ultra-thin perfect absorber employing a tunable phase change material. *Appl. Phys. Lett.* **101,** 221101 (2012).
24. Hecht, E. *Optics* 4th edn (Addison-Wesley, 2001).
25. Huang, F. M. & Zheludev, N. I. Super-resolution without evanescent waves. *Nano Lett.* **9,** 1249–1254 (2009).
26. Biagioni, P. *et al.* Near-field polarization shaping by a near-resonant plasmonic cross antenna. *Phys. Rev. B* **80,** 153409 (2009).
27. Jiang, Z. H. *et al.* Tailoring dispersion for broadband low-loss optical metamaterials using deep-subwavelength inclusions. *Sci. Rep.* **3,** 1571 (2013).
28. Monticone, F., Estakhri, N. M. & Alù, A. Full control of nanoscale optical transmission with a composite metascreen. *Phys. Rev. Lett.* **110,** 203903 (2013).
29. Pfeiffer, C. & Grbic, A. Metamaterial Huygens' surfaces: Tailoring wave fronts with reflectionless sheets. *Phys. Rev. Lett.* **110,** 197401 (2013).
30. Maier, S. A. *Plasmonics: Fundamentals and Applications* (Springer, 2007).
31. Feynman, R. P., Leighton, R. B. & Sands, M. *The Feynman Lectures on Physics* (Addison Wesley Longman, 1970).
32. Aieta, F. *et al.* Out-of-plane reflection and refraction of light by anisotropic optical antenna metasurfaces with phase discontinuities. *Nano Lett.* **12,** 1702–1706 (2012).
33. Ni, X., Emani, N. K., Kildishev, A. V., Boltasseva, A. & Shalaev, V. M. Broadband light bending with plasmonic nanoantennas. *Science* **335,** 427 (2012).
34. Yu, N. *et al.* A broadband, background-free quarter-wave plate based on plasmonic metasurfaces. *Nano Lett.* **12,** 6328–6333 (2012).
35. Kats, M. A. *et al.* Giant birefringence in optical antenna arrays with widely tailorable optical anisotropy. *Proc. Natl Acad. Sci. USA* **109,** 12364–12368 (2012).
36. Larouche, S. & Smith, D. R. Reconciliation of generalized refraction with diffraction theory. *Opt. Lett.* **37,** 2391–2393 (2012).
37. Sun, S. *et al.* High-efficiency broadband anomalous reflection by gradient meta-surfaces. *Nano Lett.* **12,** 6223–6229 (2012).
38. Sun, S. *et al.* Gradient-index meta-surfaces as a bridge linking propagating waves and surface waves. *Nature Mater.* **11,** 426–431 (2012).
39. Farmahini-Farahani, M. & Mosallaei, H. Birefringent reflectarray metasurface for beam engineering in infrared. *Opt. Lett.* **38,** 462–464 (2013).
40. Parker, D. & Zimmermann, D. C. Phased arrays - part 1: Theory and architectures. *IEEE Trans. Microwave Theory Tech.* **50,** 678–687 (2002).
41. Parker, D. & Zimmermann, D. C. Phased arrays-part II: Implementations, applications, and future trends. *IEEE Trans. Microwave Theory Tech.* **50,** 688–698 (2002).
42. Aieta, F. *et al.* Aberration-free ultrathin flat lenses and axicons at telecom wavelengths based on plasmonic metasurfaces. *Nano Lett.* **12,** 4932–4936 (2012).

43. Ni, X., Ishii, S., Kildishev, A. V. & Shalaev, V. M. Ultra-thin, planar, Babinet-inverted plasmonic metalenses. *Light: Sci. Appl.* **2,** e27 (2013).
44. Memarzadeh, B. & Mosallaei, H. Array of planar plasmonic scatterers functioning as light concentrator. *Opt. Lett.* **36,** 2569–2571 (2011).
45. Pors, A., Nielsen, M. G., Eriksen, R. L. & Bozhevolnyi, S. I. Broadband focusing flat mirrors based on plasmonic gradient metasurfaces. *Nano Lett.* **13,** 829–834 (2013).
46. Genevet, P. *et al.* Ultra-thin plasmonic optical vortex plate based on phase discontinuities. *Appl. Phys. Lett.* **100,** 013101 (2012).
47. Nye, J. F. & Berry, M. V. Dislocations in wave trains. *Proc. R. Soc. Lond. A* **336,** 165–190 (1974).
48. Padgett, M., Courtial, J. & Allen, L. Light's orbital angular momentum. *Phys. Today* **57,** 35–40 (2004).
49. Lawrence, N., Trevino, J. & Dal Negro, L. Aperiodic arrays of active nanopillars for radiation engineering. *J. Appl. Phys.* **111,** 113101 (2012).
50. Pancharatnam, S. Generalized theory of interference, and its applications. Part I. Coherent pencils. *Proc. Indian Acad. Sci. Sect. A* **44,** 247–262 (1956).
51. Berry, M. V. Quantal phase factors accompanying adiabatic changes. *Proc. R. Soc. London A* **392,** 45–57 (1984).
52. Kang, M., Chen, J., Wang, X.-L. & Wang, H.-T. Twisted vector field from an inhomogeneous and anisotropic metamaterial. *J. Opt. Soc. Am. B* **29,** 572–576 (2012).
53. Yariv, A. *Optical Electronics in Modern Communications* 5th edn (Oxford Univ. Press, 1997).
54. Kang, M., Feng, T., Wang, H.-T. & Li, J. Wave front engineering from an array of thin aperture antennas. *Opt. Express* **14,** 15882–15890 (2012).
55. Chen, X. *et al.* Dual-polarity plasmonic metalens for visible light. *Nature Commun.* **3,** 1198 (2012).
56. Huang, L. *et al.* Dispersionless phase discontinuities for controlling light propagation. *Nano Lett.* **12,** 5750–5755 (2012).
57. Shitrit, N., Bretner, I., Gorodetski, Y., Kleiner, V. & Hasman, E. Optical spin Hall effects in plasmonic chains. *Nano Lett.* **11,** 2038–2042 (2011).
58. Cowan, J. J. The surface plasmon resonance effect in holography. *Opt. Comm.* **5,** 69–72 (1972).
59. Ozaki, M., Kato, J.-I. & Kawata, S. Surface-plasmon holography with white-light illumination. *Science* **332,** 218–220 (2011).
60. Tetienne, J.-P. *et al.* Dipolar modeling and experimental demonstration of multi-beam plasmonic collimators. *New J. Phys.* **13,** 053057 (2011).
61. Genevet, P., Lin, J., Kats, M. A. & Capasso, F. Holographic detection of the orbital angular momentum of light with plasmonic photodiodes. *Nature Commun.* **3,** 1278 (2012).
62. Dolev, I., Epstein, I. & Arie, A. Surface-plasmon holographic beam shaping. *Phys. Rev. Lett.* **109,** 203903 (2012).
63. Fong, B. H., Colburn, J. S., Ottusch, J. J., Visher, J. L. & Sievenpiper, D. F. Scalar and tensor holographic artificial impedance surfaces. *IEEE Trans. Antenna Propag.* **58,** 3212–3221 (2010).
64. Minatti, G., Caminita, F., Casaletti, M. & Maci, S. Spiral leaky-wave antennas based on modulated surface impedance. *IEEE Trans. Antenna Propag.* **59,** 4436–4444 (2011).
65. Qazilbash, M. M. *et al.* Mott transition in VO_2 revealed by infrared spectroscopy and nano-imaging. *Science* **318,** 1750–1753 (2007).
66. Streyer, W., Law, S., Rooney, G., Jacobs, T. & Wasserman, D. Strong absorption and selective emission from engineered metals with dielectric coatings. *Opt. Express* **21,** 9113–9122 (2013).
67. Dotan, H. *et al.* Resonant light trapping in ultrathin films for water splitting. *Nature Mater.* **12,** 158–164 (2013).
68. Minoshima, K., Kowalevicz, A. M., Hartl, I., Ippen, E. P. & Fujimoto, J. G. Photonic device fabrication in glass by use of nonlinear materials processing with a femtosecond laser oscillator. *Opt. Lett.* **26,** 1516–1518 (2001).
69. Calvert, P. Inkjet printing for materials and devices. *Chem. Mater.* **13,** 3299–3305 (2001).
70. Streppel, U. *et al.* New wafer-scale fabrication method for stacked optical waveguide interconnects and 3D micro-optic structures using photoresponsive (inorganic–organic hybrid) polymers. *Opt. Mater.* **21,** 475–483 (2002).
71. Miklyaev, Y. V. *et al.* Three-dimensional face-centered-cubic photonic crystal templates by laser holography: fabrication, optical characterization, and band-structure calculations. *Appl. Phys. Lett.* **82,** 1284–1286 (2003).
72. Gansel, J. K. *et al.* Gold helix photonic metamaterial as broadband circular polarizer. *Science* **325,** 1513–1515 (2009).
73. Kress, B. C. & Meyrueis, P. *Digital Diffractive Optics: An Introduction to Planar Diffractive Optics and Related Technology* (Wiley, 2000).
74. Li, G. *et al.* Switchable electro-optic diffractive lens with high efficiency for ophthalmic applications. *Proc. Natl Acad. Sci. USA* **103,** 6100–6104 (2006).
75. Leger, J. R., Swanson, G. J. & Veldkamp, W. B. Coherent laser addition using binary phase gratings. *Appl. Opt.* **26,** 4391–4399 (1987).
76. Bifano, T. G., Perreault, J., Mali, R. K. & Horenstein, M. N. Microelectromechanical deformable mirrors. *IEEE J. Sel. Top. Quantum Electron.* **5,** 83-89 (1999).
77. Wu, M. C., Solgaard, O. & Ford, J. E. Optical MEMS for lightwave communication. *J. Lightwave Technol.* **24,** 4433–4454 (2006).
78. Neto, L. G., Cardona, P. S. P., Cirino, G. A., Mansano, R. D. & Verdonck, P. Design, fabrication, and characterization of a full complex-amplitude modulation diffractive optical element. *J. Micro-Nanolithogr. MEMS MOEMS* **2,** 96–104 (2003).
79. Kley, E.-B., Schnabel, B. & Zeitner, U. D. E-beam lithography — an efficient tool for the fabrication of diffractive and microoptical elements. *Proc. SPIE* **3008,** 222–232 (1997).
80. Pedder, J. E. A., Holmes, A. S., Allott, R. & Boehlen, K. Pulsed laser ablation for volume micro-optical arrays on large area substrates. *Proc. SPIE* **6462,** 64620W-1–64620W-7 (2007).
81. Gale, M. T., Rossi, M. & Schütz, H. Fabrication of continuous-relief micro-optical elements by direct laser writing in photoresist. *Proc. SPIE* **2045,** 54–62 (2005).
82. Suleski, T. J. & O'Shea, D. C. Gray-scale masks for diffractive-optics fabrication: I. Commercial slide imagers. *Appl. Opt.* **34,** 7507–7517 (1995).
83. O'Shea, D. C. & Rockward, W. S. Gray-scale masks for diffractive-optics fabrication: II. Spatially filtered halftone screens. *Appl. Opt.* **34,** 7518–7526 (1995).
84. Maruo, S., Nakamura, O. & Kawata, S. Three-dimensional microfabrication with two-photon-absorbed photopolymerization. *Opt. Lett.* **22,** 132–134 (1997).
85. Cumpston, B. H. *et al.* Two-photon polymerization initiators for three-dimensional optical data storage and microfabrication. *Nature* **398,** 51–54 (1999).
86. Vora, K., Kang, S., Shukla, S. & Mazur, E. Fabrication of disconnected three dimensional silver nanostructures in a polymer matrix. *Appl. Phys. Lett.* **100,** 063120 (2012).
87. Suhara, T., Kobayashi, K., Nishihara, H. & Koyama, J. Graded-index Fresnel lenses for integrated optics. *Appl. Opt.* **21,** 1966–1971 (1982).
88. Chen, F. T. & Craighead, H. G. Diffractive phase elements based on two-dimensional artificial dielectrics. *Opt. Lett.* **20,** 121–123 (1995).
89. Mait, J. N., Prather, D. W. & Mirotznik, M. S. Binary subwavelength diffractive-lens design. *Opt. Lett.* **23,** 1343–1345 (1998).
90. Valentine, J., Li, J., Zentgraf, T., Bartal, G. & Zhang, X. An optical cloak made of dielectrics. *Nature Mater.* **8,** 568–571 (2009).
91. Gao, H., Zhang, B., Johnson, S. G. & Barbastathis, G. Design of thin–film photonic metamaterial Lüneburg lens using analytical approach. *Opt. Express* **20,** 1617–1628 (2012).
92. Herzig, H. P. *Micro-Optics: Elements, Systems and Applications* (Taylor & Francis, 1997).
93. Smythe, E. J., Dickey, M. D., Whitesides, G. M. & Capasso, F. A technique to transfer metallic nanoscale patterns to small and non-planar surfaces. *ACS Nano* **3,** 59–65 (2009).
94. Mason, J. A., Smith, S. & Wasserman, D. Strong absorption and selective thermal emission from a midinfrared metamaterial. *Appl. Phys. Lett.* **98,** 241105 (2011).
95. Chen, H.-T. *et al.* Active terahertz metamaterial devices. *Nature* **444,** 597–600 (2006).
96. Ju, L. *et al.* Graphene plasmonics for tunable terahertz metamaterials. *Nature Nanotech.* **6,** 630–634 (2011).
97. Vakil, A. & Engheta, N. Transformation optics using graphene. *Science* **332,** 1291–1294 (2011).
98. Fallahi, A. & Perruisseau-Carrier, J. Design of tunable biperiodic graphene metasurfaces. *Phys. Rev. B* **86,** 195408 (2012).
99. Carrasco, E., Tamagnone, M. & Perruisseau-Carrier, J. Tunable graphene reflective cells for THz reflectarrays and generalized law of reflection. *Appl. Phys. Lett.* **102,** 104103 (2013).
100. Yao, Y. *et al.* Broad electrical tuning of graphene-loaded plasmonic antennas. *Nano Lett.* **13,** 1257–1264 (2013).
101. Li, Z. & Yu, N. Modulation of mid-infrared light using graphene-metal plasmonic antennas. *Appl. Phys. Lett.* **102,** 131108 (2013).
102. Fang, Z. *et al.* Gated tunability and hybridization of localized plasmons in nanostructured graphene. *ACS Nano* **7,** 2388–2395 (2013).
103. Kats, M. A. *et al.* Thermal tuning of mid-infrared plasmonic antenna arrays using a phase change material. *Opt. Lett.* **38,** 368–370 (2013).
104. Gu, J. *et al.* Active control of electromagnetically induced transparency analogue in terahertz metamaterials. *Nature Commun.* **3,** 1151 (2012).
105. Shadrivov, I. V., Kapitanova, P. V., Maslovski, S. I. & Kivshar, Y. S. Metamaterials controlled with light. *Phys. Rev. Lett.* **109,** 083902 (2012).
106. Wang, X., Belyanin, A. A., Crooker, S. A., Mittleman, D. M. & Kono, J. Interference-induced terahertz transparency in a magneto-plasma in a semiconductor. *Nature Phys.* **6,** 126–130 (2010).

107. Pryce, I. M., Aydin, K., Kelaita, Y. A., Briggs, R. M. & Atwater, H. A. Highly strained compliant optical metamaterials with large frequency tunability. *Nano Lett.* **10,** 4222–4227 (2010).
108. Sun, J., Timurdogan, E., Yaacobi, A., Hosseini, E. S. & Watts, M. R. Large-scale nanophotonic phased array. *Nature* **493,** 195–199 (2013).

Acknowledgements

The authors acknowledge the contributions of Z. Gaburro, P. Genevet, M. A. Kats, F. Aieta, R. Blanchard, J. Lin, J.-P. Tetienne, G. Aoust, D. Sharma, Z. Yang, S. Ramanathan, M. Mumtaz Qazilbash and D. N. Basov to the research reviewed in this article. Quantum cascade laser materials were provided by Hamamatsu Photonics KK. The authors acknowledge support from the Harvard Nanoscale Science and Engineering Center (NSEC) under contract NSF/PHY 06-46094, and the Center for Nanoscale Systems (CNS) at Harvard University, which is a member of the National Nanotechnology Infrastructure Network (NNIN). This work was supported in part by the Defense Advanced Research Projects Agency (DARPA) N/MEMS S&T Fundamentals program under Grant N66001-10-1-4008 issued by the Space and Naval Warfare Systems Center Pacific (SPAWAR) and by the Air Force Office of Scientific Research under grant number FA9550-12-1-0289. N.Y. acknowledges funding provided by the Fu Foundation School of Engineering and Applied Science, and the Department of Applied Physics and Applied Mathematics, Columbia University.

Additional information

Reprints and permissions information is available online at www.nature.com/reprints. Correspondence should be addressed to N.Y. or F.C.

Competing financial interests

The authors declare no competing financial interests.